

Temperature effects in topological insulators of transition metal dichalcogenide monolayers

Siyu Chen,^{1,*} Isaac J. Parker,² and Bartomeu Monserrat^{1,3,†}

¹*TCM Group, Cavendish Laboratory, University of Cambridge,
J. J. Thomson Avenue, Cambridge CB3 0HE, United Kingdom*

²*Gonville and Caius College, University of Cambridge,
Trinity Street, Cambridge CB2 1TA, United Kingdom*

³*Department of Materials Science and Metallurgy, University of Cambridge,
27 Charles Babbage Road, Cambridge CB3 0FS, United Kingdom*

We investigate the role of temperature on the topological insulating state of metal dichalcogenide monolayers, $1T'-MX_2$ ($M=W, Mo$ and $X=S, Se$). Using first principles calculations based on density functional theory, we consider three temperature-related contributions to the topological band gap: electrons coupling with short-wavelength phonons, with long-wavelength phonons *via* Fröhlich coupling, and thermal expansion. We find that electron-phonon coupling promotes the topology of the electronic structures of all $1T'-MX_2$ monolayers, while thermal expansion acts as a counteracting effect. Additionally, we derive the band renormalization from Fröhlich coupling in the two-dimensional context and observe its relatively modest contribution to $1T'-MX_2$ monolayers. Finally, we present a simplified physical picture to understand the “inverse Varshni” effect driven by band inversion in topological insulators. Our work reveals that, among the four $1T'-MX_2$ studied monolayers, $MoSe_2$ is a promising candidate for room temperature applications as its band gap displays remarkable resilience against thermal expansion, while the topological order of WS_2 can be tuned under the combined influence of strain and temperature. Both materials represent novel examples of temperature promoted topological insulators.

I. INTRODUCTION

In condensed matter physics, the unique electronic properties of topological insulators have sparked immense interest, captivating the scientific community with their potential to redefine the landscape of electronic and quantum computing technologies. Over the past two decades, significant advancements have been made in unravelling the fundamental features of topological insulators and in the manipulation of their distinctive properties [1–8].

The manipulation of topologically non-trivial band gaps has emerged as a highly active research direction. These manipulations have been achieved through various means, including alterations in chemical composition [9, 10], the application of external pressure [11, 12], the imposition of mechanical strain [13–15], and the influence of electromagnetic fields [16–18]. Recent attention within the scientific community has shifted towards exploring the intriguing possibility of controlling the topological characteristics of these materials through temperature, both in theory [19–28] and experiments [29–37].

Despite this burgeoning interest, a comprehensive examination of the interplay between temperature and the unique electronic states of topological insulators remains a relatively under-explored frontier. So far, most works indicate that increasing temperature suppresses the topological phase, in the sense that the topological band gap

decreases with increasing temperature [21, 23, 25, 26, 28, 36, 37]. In particular, thermal expansion is often responsible for the ultimate suppression of topological order, as it drives the system towards the atomic limit. This suggests that a generic topological phase diagram as a function of temperature is one with a low temperature topological phase and a high temperature normal phase. Indeed, several reports describe the reduction of the topological band gap with increasing temperature culminating in a transition from a topological (crystalline) insulator into a normal insulator [21, 25, 26, 30] or from a strong topological insulator into a weak topological insulator [23, 36, 37]. It has been argued that electron-phonon interactions can promote a topological insulating phase with increasing temperature in $BiTlS$ [22] and bismuthene [27], but these works neglect thermal expansion so the overall temperature dependence in these materials remains an open question. As far as we are aware, the only compound in which temperature has been shown to promote topological order, specifically a topological semimetallic phase, is PbO_2 [24], and there are no examples in which increasing temperature promotes a topological insulating phase.

Motivated by the paucity of reports on materials where temperature promotes topological insulating states, in this work we systematically study the interplay between temperature and topology in four transition metal dichalcogenide (TMD) monolayers $1T'-MX_2$ (where $M=W, Mo$ and $X=Se$ and S). The motivation behind the choice of monolayer TMDs for our study is two-fold. First, monolayer materials often exhibit unconventional thermal effects, including weak or negative thermal expansion, which may minimize the detrimental

* sc2090@cam.ac.uk

† bm418@cam.ac.uk

tal effects of thermal expansion on topological order observed in most compounds. Second, these specific TMD monolayers have been shown to be a realization of topological insulators at 0 K [38, 39], but their behavior at finite temperature is still an open question.

Our investigation illustrates the pivotal role played by electron-phonon coupling and thermal expansion in influencing the topology of the electronic structures of 1T'-MX₂ monolayers. Particularly noteworthy are MoSe₂ and WS₂, which stand out as the first example of temperature promoted topological insulators. The former emerges as a promising candidate for room temperature applications, owing to its remarkable resistance to thermal expansion, while the latter exhibits a tunable topological behavior when subjected to the combined influence of strain and temperature. Overall, our findings enrich the family of materials where temperature can promote topology.

The paper is organized as follows. In Section II, we present the theory of finite temperature band structures and its first principles implementation in the context of the finite difference method. In Section III, we apply the method to investigate 1T'-MX₂, showcasing the competition between electron-phonon coupling and thermal expansion. In Section IV, we propose a simple model that aids in understanding the circumstances under which electron-phonon coupling can promote the topological phase in the presence of significant band inversion. In Section V, we show the topological order of WS₂ can be manipulated through a combination of strain and temperature, illustrating a transition from a low temperature normal to a high temperature topological phase. Finally, we summarize the contributions and findings of our research in Section VI.

II. TEMPERATURE DEPENDENT TOPOLOGICAL BAND GAP

A topological phase transition induced by temperature from a topological insulator to a trivial insulator (or the other way around) requires the bulk band gap to re-order. In the case of centrosymmetric materials, the band re-ordering is mediated by a gapless Dirac semimetal phase [40], where the Dirac cone is located at one of the time reversal invariant momenta points. Therefore, the key to exploring the role of temperature in topological insulators is to consider the temperature dependence of certain energy eigenvalues.

The temperature dependent eigenenergy, $E_{n\mathbf{k}}(T)$, of a single electron with band index n and wavevector \mathbf{k} can be approximated by the sum of two independent contributions: the renormalization of the eigenenergy by electron-phonon interactions, $\Delta E_{n\mathbf{k}}^{\text{EP}}(T)$; and by thermal expansion, $\Delta E_{n\mathbf{k}}^{\text{TE}}(T)$. For practical calculation reasons, the former needs to be further decomposed into the short- and long-wavelength phonon contributions, $\Delta E_{n\mathbf{k}}^{\text{S}}(T)$, and $\Delta E_{n\mathbf{k}}^{\text{L}}(T)$, each treated separately. Overall, the total

shift of the electron eigenenergy at temperature T reads

$$\Delta E_{n\mathbf{k}}(T) = \Delta E_{n\mathbf{k}}^{\text{S}}(T) + \Delta E_{n\mathbf{k}}^{\text{L}}(T) + \Delta E_{n\mathbf{k}}^{\text{TE}}(T). \quad (1)$$

In the following subsections, we discuss each contribution in turn. We use atomic units, $\hbar = e = m_{\text{el}} = 4\pi\epsilon_0 = 1$, unless otherwise stated.

A. Band gap renormalized by short-wavelength phonons

The investigation of band renormalization through coupling electrons to short-wavelength phonons has a long history, culminating in the well-established Allen-Heine-Cardona (AHC) theory [41–43]. The AHC theory can be reformulated in a manner that can readily lend itself to implementation within the first-principles finite difference method:

$$\Delta E_{n\mathbf{k}}^{\text{S}}(T) = \frac{1}{2} \sum_{\nu\mathbf{q}} \frac{1}{2\omega_{\nu\mathbf{q}}} \frac{\partial^2 E_{n\mathbf{k}}}{\partial \mu_{\nu\mathbf{q}}^2} [1 + 2n_{\text{B}}(\omega_{\nu\mathbf{q}}, T)], \quad (2)$$

where $\omega_{\nu\mathbf{q}}$ is the frequency of a phonon with the branch number ν and wavevector \mathbf{q} , $\mu_{\nu\mathbf{q}}$ is the real-valued phonon displacement (see the detailed definition in Eqs. (A1) and (A4)), and $n_{\text{B}}(\omega_{\nu\mathbf{q}}, T) = [\exp(\frac{\omega_{\nu\mathbf{q}}}{k_{\text{B}}T}) - 1]^{-1}$ is the Bose-Einstein factor. It is worth noting that there is a nonzero correction to the energy band even at zero temperature with the vanishing Bose-Einstein factor, arising from the zero-point motion of the ions as a purely quantum effect. We refer readers who are interested in the rigorous mathematical derivations of the theory to Refs. [41–46], where the same results have been obtained through alternative approaches. We show the equivalence between our formulation and others in Appendix A.

B. Band gap renormalized by long-wavelength phonons

In principle, Eq. (2) captures the coupling between electrons and *all*-wavelength phonons. However, in practice, explicitly accessing the \mathbf{q} -points close to the center of the Brillouin zone can become computationally prohibitive due to the inherent incompatibility of the long-wavelength limit with the Born-von-Kármán periodic boundary condition. As a result, accounting for the band gap renormalization contributed by long-wavelength phonons requires a separate treatment.

Specifically, in the long-wavelength limit, the significance of atomic-scale interactions diminishes, and electrons can be regarded as becoming coupled with the macroscopic electric field induced by longitudinal optical phonons. This mechanism is known as the Fröhlich interaction [47, 48]. It is especially crucial in the case of ionic crystals, where the interaction has been shown to be

strong enough to significantly influence physical phenomena such as electron lifetimes and carrier mobilities [49].

Nery and Allen derived an analytical expression to address the missing portion of the contribution associated with the long-wavelength optical phonon modes for three-dimensional (3D) materials [50]. Following a similar methodology, combined with the latest results on polarons in two-dimensional (2D) systems [51, 52], we have derived the corresponding band gap renormalization for a 2D material:

$$\Delta E_{n\mathbf{k}}^{\text{L}}(T) = \int_0^\infty dq \frac{1}{2} m^* q_0^2 d \omega_{\text{LO}} (\epsilon_0 - \epsilon_\infty) \frac{q}{(q_0 + q)^2} \left[\frac{1 + n_{\text{B}}(\omega_{\text{LO}}, T)}{-q^2 - 2m^* \omega_{\text{LO}}} + \frac{n_{\text{B}}(\omega_{\text{LO}}, T)}{-q^2 + 2m^* \omega_{\text{LO}}} \right]. \quad (3)$$

Here, m^* is the effective mass of the band, q_0 is a characteristic wavevector of the polaron in 2D materials (defined in Eq. (B6) and Refs. [51, 52]), d is the effective thickness of the 2D material, ω_{LO} is the frequency of the longitudinal-optical phonon, and ϵ_∞ and ϵ_0 are the high-frequency and static relative permittivities, respectively. The details of the derivation are presented in Appendix B, where, very interestingly, we find that the dimensionality change from three to two significantly amplifies the mathematical intricacy involved in band renormalization.

C. Thermal expansion

In the context of experimentally probing the temperature dependent electron eigenenergy, a prevailing practice entails the execution of experiments under constant-pressure conditions. Therefore, it is necessary to also include the influence of thermal expansion on electron eigenenergies, which has been shown to make a comparable contribution to electron-phonon coupling in three dimensional topological materials [21]. The temperature dependence of the electron eigenenergy induced by thermal expansion can be expressed as [42, 43]:

$$\Delta E_{n\mathbf{k}}^{\text{TE}}(T) = \int_0^T dT \left(\frac{\partial E_{n\mathbf{k}}}{\partial V} \right)_{T_0} \left(\frac{\partial V}{\partial T} \right)_{P_0}. \quad (4)$$

Here, $\left(\frac{\partial E_{n\mathbf{k}}}{\partial V} \right)_{T_0}$ represents the eigenenergy shift as the system volume changes at constant temperature T_0 , and $\left(\frac{\partial V}{\partial T} \right)_{P_0}$ represents the volume change as the system temperature increases at constant pressure P_0 .

D. First-principles implementation

To calculate band renormalization induced by short-wavelength phonons from first principles, we use Eq. (2) as our starting point. This choice (instead of Eq. (A6)) enables us to bypass the explicit calculation of the electron-phonon coupling matrix elements. The only

terms that need to be numerically evaluated are the second order derivatives of the band structure with respect to the displacement of each phonon. We implement this in the finite difference context using a three-point central formula:

$$\frac{\partial^2 E_{n\mathbf{k}}}{\partial \mu_{\nu\mathbf{q}}^2} \simeq \frac{E_{n\mathbf{k}}^{(+\delta\mu_{\nu\mathbf{q}})} + E_{n\mathbf{k}}^{(-\delta\mu_{\nu\mathbf{q}})} - 2E_{n\mathbf{k}}^{(0)}}{\delta\mu_{\nu\mathbf{q}}^2}, \quad (5)$$

where $E_{n\mathbf{k}}^{(+\delta\mu_{\nu\mathbf{q}})}$ represents the band structure calculated by incorporating a ‘‘frozen’’ phonon characterized by ν and \mathbf{q} with a real displacement of $+\delta\mu_{\nu\mathbf{q}}$. In the case of degenerate band structures, the above second derivatives are averaged over all degenerate states. The BZ integration required by Eq. (2) is implemented by invoking the non-uniform \mathbf{q} -point sampling and nondiagonal supercell techniques [27, 53] to ensure optimal efficiency.

To calculate band renormalization induced by long-wavelength phonons, we employ Cauchy’s principal value integration to evaluate Eq. (3), circumventing the divergence arising from the singularity in the integrand when $-q^2 \pm 2m^* \omega_{\text{LO}} = 0$. We note that Ref. [50] proposed the alternative approach of invoking the adiabatic approximation to merge the two singularities into one and shifting them off the real axis by an amount $i\eta$. Although we have also derived the counterpart for 2D materials following the same idea (as shown in Eq. (B7)), which might provide accurate results with a less dense \mathbf{q} -point grid when $i\eta$ is judiciously chosen, we opt not to adopt this approach in this work to avoid introducing the *ad hoc* parameter. All the parameters within Eq. (3) can be acquired through well-established first-principle methods. For instance, m^* can be determined by fitting the curvature of the band, while ϵ_∞ and ϵ_0 can be calculated by assessing the response of the system to an applied electric field.

To model thermal expansion from first principles through $\left(\frac{\partial V}{\partial T} \right)_{P_0}$ in Eq. (4), we use the quasi-harmonic approximation to incorporate the volume dependence of phonon frequencies, such that the Helmholtz free energy of the vibrating lattice can be expressed as [54]:

$$F(V; T) = U(V; 0) + k_{\text{B}} T \sum_{\nu\mathbf{q}} \ln \left[2 \sinh \left(\frac{\omega_{\nu\mathbf{q}}(V)}{2k_{\text{B}} T} \right) \right], \quad (6)$$

where the first term is the potential energy for the static lattice and the second term is the vibrational contribution to the free energy. It is worth noting that the second term does not vanish at zero temperature; instead, it equals $\frac{1}{2} \sum_{\nu\mathbf{q}} \omega_{\nu\mathbf{q}}(V)$, which leads to the contribution from zero-point motion to thermal expansion. We further implement Eq. (6) by calculating the system of interest at a few volumes in the expansion and compression regime. At each volume, the static lattice potential energy $U(V; 0)$ can be obtained through a lattice-constrained geometry optimisation, and the volume-dependent phonon frequency $\omega_{\nu\mathbf{q}}(V)$ can be obtained from the corresponding phonon calculations. By

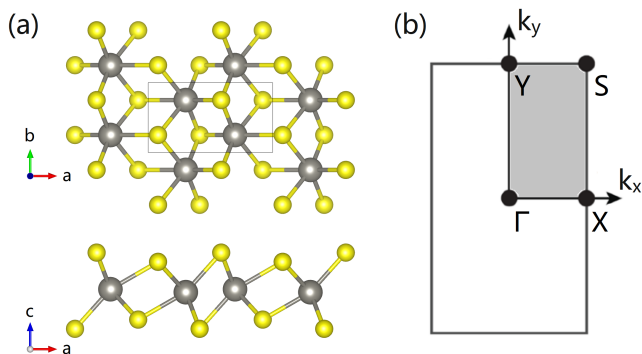


FIG. 1. (a) Crystal structure of $1T'$ - MX_2 and (b) its BZ. The gray and yellow balls represent the $M=W, Mo$ and $X=S, Se$ atoms respectively. The gray shaded area represents the irreducible Brillouin zone.

fitting the resulting Helmholtz free energy $F(V; T)$ with a polynomial function, we determine the volume corresponding to the minimum of $F(V; T)$ for a given temperature T , that is, the equilibrium volume at that temperature.

III. RESULTS AND DISCUSSION

A. Crystal structure

Monolayer TMDs have been confirmed to exhibit a series of stable and metastable phases, both in theory and experiments [55, 56]. Of particular interest within this work is the $1T'$ -phase, which adopts a monoclinic structure characterized by the space group $P2_1/m$. Figure 1(a) visualizes the crystallographic structure from both top and side perspectives. The structure emerges as a spontaneous symmetry breaking from the $1T$ -phase (with space group $P\bar{3}m1$) induced by the Peierls instability in which the M-M dimerization takes place thereby eliminating the degeneracy of the states near the Fermi level and lowering the energy of the system. Despite the distortion of M atoms leading to the loss of certain symmetries, the $1T'$ -phase still possesses an inversion centre, a mirror plane and a two-fold screw axis. Therefore, its irreducible Brillouin zone is a quarter of the whole Brillouin zone, as depicted in Fig. 1(b).

B. Computational details

We perform first-principles calculations at the density functional theory (DFT) level [57, 58] with the Vienna *ab initio* Simulation Package (VASP) [59]. A vacuum layer with a thickness of 20 Å is used in the calculation to avoid periodic image interactions along the direction perpendicular to the plane. The interaction between ions and valence electrons is modeled with pseudopo-

		WS ₂	WSe ₂	MoS ₂	MoSe ₂
ΔE^S	static	183 meV	693 meV	531 meV	713 meV
	0 K	+17 meV	+5 meV	+4 meV	+8 meV
ΔE^L	300 K	+38 meV	+17 meV	+17 meV	+21 meV
	0 K	-8 meV	-5 meV	-2 meV	-5 meV
ΔE^{TE}	300 K	-8 meV	-5 meV	-1 meV	-5 meV
	0 K	-4 meV	-3 meV	-2 meV	-0.4 meV
	300 K	-17 meV	-16 meV	-13 meV	-1 meV

TABLE I. Static and renormalized band gap of WS₂, WSe₂, MoS₂, and MoSe₂ at $T = 0$ K and 300 K. The total renormalization is equal to the sum of the renormalization induced by short- and long-wavelength phonons, $\Delta E^S(T)$ and $\Delta E^L(T)$, and the thermal expansion, $\Delta E^{TE}(T)$.

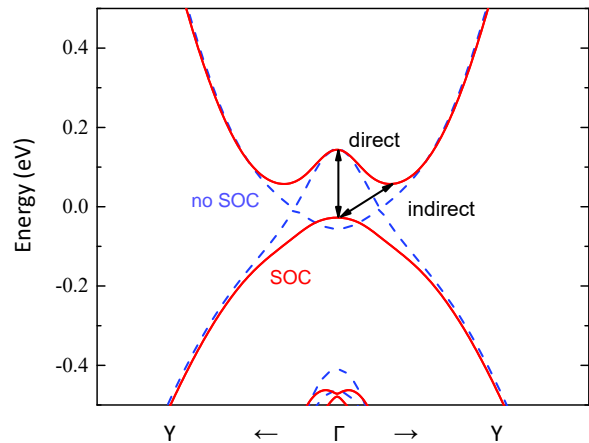


FIG. 2. Band structures of WS₂ with and without spin-orbit coupling (SOC) in the vicinity of the Γ point. The direct and indirect gaps are highlighted, where the former corresponds to the inverted band gap in the context of topological insulators.

tentials based on the projector-augmented wave [60, 61] method, where the valence electrons of the transition metals are $ns^2(n-1)d^5$ (where $n = 6$ for $M=W$ and $n = 5$ for $M=Mo$) and the valence electrons of chalcogen are ns^2np^4 (where $n = 4$ for $X=Se$ and $n = 3$ for $X=S$). The exchange-correlation functional is treated in the generalized gradient approximation parametrized by Perdew-Burke-Ernzerhoff (PBE) [62]. An energy cut-off of 500 eV for the plane-wave expansion and a Γ -centered \mathbf{k} -point grid of size $5 \times 9 \times 1$ for Brillouin zone integration are adopted in the calculations. The spin-orbit coupling is included in the calculations *via* a perturbation to the scalar relativistic Hamiltonian [63].

C. Electronic structures

It has been confirmed both in theory and experiments that the $1T'$ - MX_2 family are topological insulators [38, 64–69]. In a broader context, the band struc-

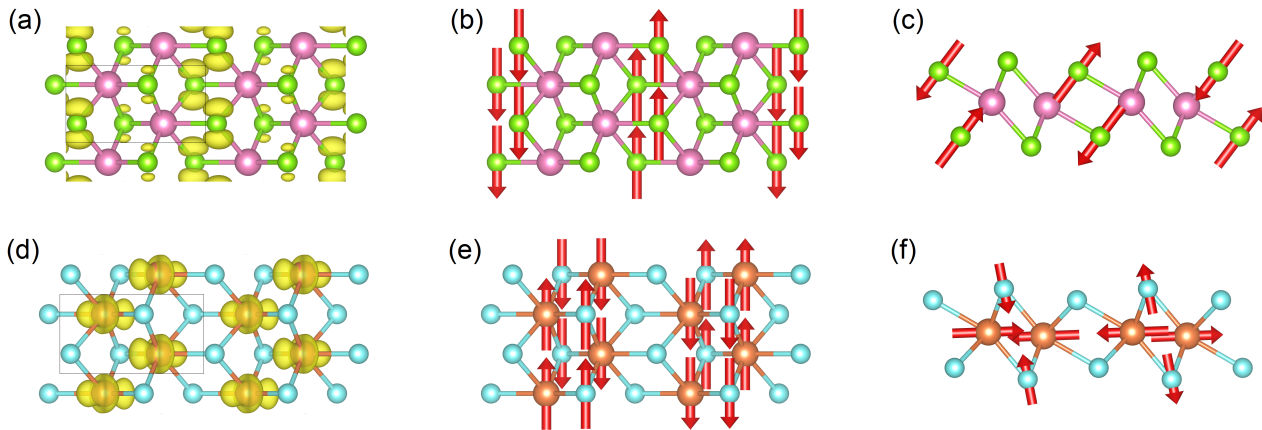


FIG. 3. Hole density of the state associated with the conduction band minimum at the Γ point, alongside two vibration modes at the X point that exhibit strong coupling with it. Panels (a-c) correspond to MoS₂, WS₂ and WSe₂, while panels (d-f) correspond to MoSe₂. The red arrows indicate the vibration of the corresponding atoms.

ture of an inversion symmetric topological insulator is generally characterized by two band gaps, the indirect band gap, which corresponds to the minimum energy to excite an electron in the material bulk, and the direct band gap, where the band inversion takes places. Using WS₂ as a representative example, we show a typical band structure of a topological insulator in Fig. 2, where the band inversion induced by spin-orbit coupling occurs at the Γ point and leads to a double-well-shaped dispersion for the conduction band.

Following Ref. [38], we refer to the direct band gap at the Γ point as the inverted band gap, which reflects the band inversion strength of MX₂. Table I summarizes the values of the inverted band gaps for WS₂, WSe₂, MoS₂, and MoSe₂ at the static DFT level, where MoSe₂ exhibits the largest gap of 713 meV while WS₂ exhibits the smallest one of 183 meV. The results agree with previous first-principles studies [38, 70].

The atomic orbital projection analysis of the inverted band gap point further reveals that the non-trivial topology of 1T'-MX₂ can be understood from the p - d band inversion picture. We find that across all four compounds, the conduction band inversion is primarily influenced by hybridization of metal d_{xz} and d_{yz} states. In the cases of MoS₂, WS₂, and WSe₂, their inverted conduction bands exhibit a similar pattern, predominantly stemming from contributions of the chalcogenide p_y orbitals. On the contrary, MoSe₂ distinguishes itself from them, displaying an inverted conduction band dominated by a mixture of Mo $d_{x^2-y^2}$ and d_{z^2} states. This state manifests a distinctly different orientation compared to the chalcogenide p_y orbitals, as shown in Figs. 3(a) and (d).

D. Band gap renormalization induced by electron-phonon coupling

To effectuate an electronic structure phase transition from a topologically nontrivial state (*i.e.* 1T'-MX₂ at 0 K) to a topologically trivial state (if exists), it is imperative for the inverted band gap at the Γ point to undergo closure. Therefore, in subsequent sections, we focus on the temperature effects on this inverted band gap. It is also worth noting that, as one of the most important manifestations of topology, the topologically protected metallic edge states which carry opposite spin polarizations are required to intersect at the Γ point because of time-reversal symmetry. The presence of a finite gap guarantees the insulating nature of the bulk and ensures that electronic transport can occur only through the topologically protected metallic edge states.

1. Short-wavelength phonon-induced band gap renormalization

To obtain the phonon-induced band gap renormalization, we first calculate the phonon spectra for the four compounds thereby determining the concrete form of real-valued operators $\frac{\partial}{\partial \mu_{\nu\mathbf{q}}}$ for them. The obtained phonon spectra also allow us to theoretically confirm the dynamical stability of MX₂ at ambient pressure as there are no imaginary vibrational modes (see Fig. S1 in Supplementary Material (SM) for details).

Figure 4(a) shows the band gap corrections ΔE^S as a function of temperature, while the specific values at both absolute zero and room temperature ($T = 300$ K) are presented in Table I. In contrast to the behavior typically observed in most semiconductors, where the band gap diminishes with rising temperature, 1T'-MX₂ exhibits an opposite trend. Across the four TMDs investigated, regardless of the distinct chemical compositions, a consis-

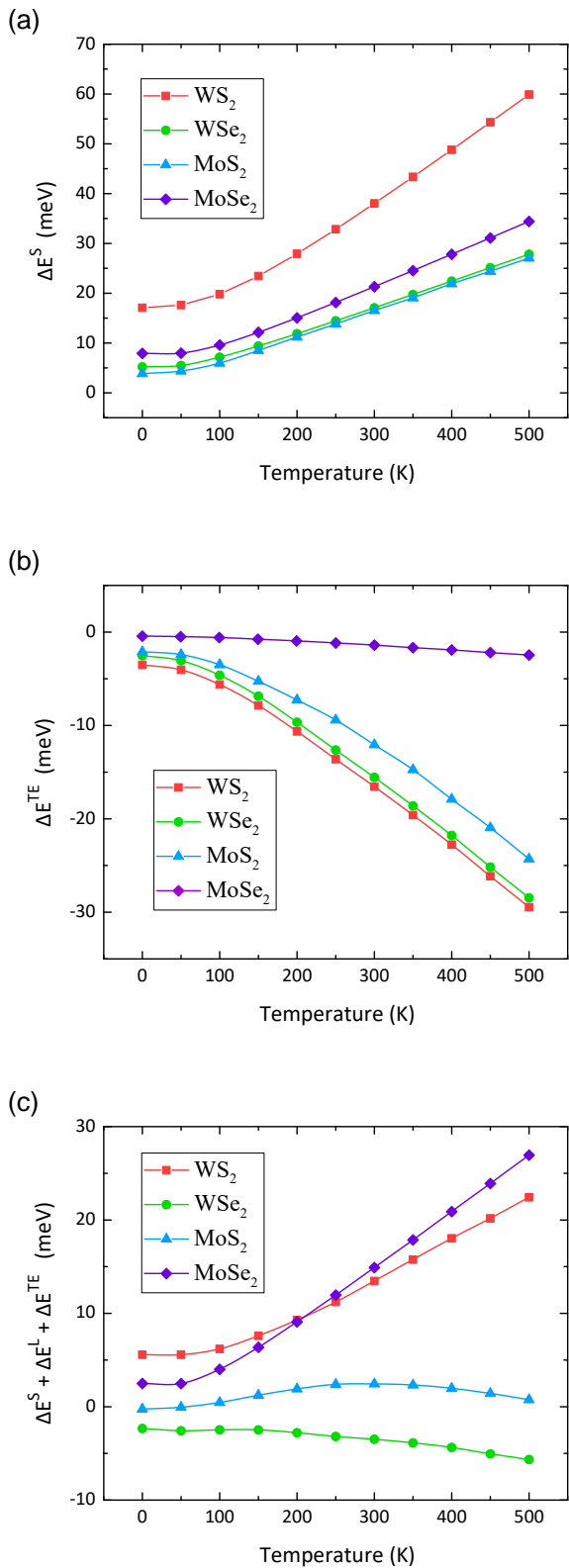


FIG. 4. Band gap renormalization as a function of temperature for WS₂, WSe₂, MoS₂ and MoSe₂, where (a) and (b) show the contribution from short-wavelength phonons, $\Delta E^S(T)$, and thermal expansion, $\Delta E^{TE}(T)$ respectively, and (c) shows the overall effect including both electron-phonon coupling and thermal expansion.

tent positive correlation between the band gap and temperature is evident. It is particularly pronounced at temperatures exceeding 100 K, showing an asymptotic linear dependence of the gap change with temperature. Below this temperature, only the low-frequency vibrational modes are excited and the phonon-induced band gap renormalization remains relatively constant. For WSe₂, MoS₂, and MoSe₂, we find that they exhibit comparable band gap corrections, around 20 meV at room temperature. In comparison, WS₂ manifests stronger electron-phonon coupling, resulting in a band gap renormalization of 38 meV, which is approximately double the values observed in the other three TMDs. This is a substantial correction, whose magnitude accounts for nearly 21% of the static band gap size in WS₂.

To have better understanding of the microscopic origin of the phonon-induced band gap renormalization, we define the electron-phonon coupling strength in the temperature dependent band structure context as

$$S_{\nu\mathbf{q}}^{\text{el-ph}} = \frac{\partial^2 E_{\text{gap}}}{\partial \mu_{\nu\mathbf{q}}^2}, \quad (7)$$

followed by the \mathbf{q} -resolved electron-phonon coupling strength defined as

$$S^{\text{el-ph}}(\mathbf{q}) = \sum_{\nu} S_{\nu\mathbf{q}}^{\text{el-ph}}. \quad (8)$$

The left bottom panels of Figs. 5 (a-d) depict the band structures for the four compounds along the high symmetry path, from which it can be seen that their conduction band minima are all located on the $\Gamma - Y$ path. For WS₂ and MoSe₂, they exhibit a (negative) parabolic and quartic shaped valence band around the Γ -point respectively, while for WSe₂ and MoS₂, their valence band manifest a double-peak shape, resulting in the valence band maximum shifting close to the conduction band maximum on the $\Gamma - Y$ path.

The left top and right panels of Figs. 5 (a-d) show the \mathbf{q} -resolved electron-phonon coupling strength along the high-symmetry path and on the whole irreducible Brillouin zone, respectively. Within the upper half-plane of the irreducible Brillouin zone, the electron-phonon coupling strength is nearly negligible. The principal contributions to the band renormalization are concentrated in proximity to the Γ and X points. Focusing on phonons at the X point, which corresponds to vibrational modes exhibiting a wavelength twice that of the original unit cell, we visualize in Figs. 3(b-c) and (e-f) the two modes that most strongly couple to the inverted band gap. Interestingly, these modes are highly localised along certain directions. For MoS₂, WS₂ and WSe₂, the dominant modes are very similar, all exclusively associated with chalcogenide atoms. One mode involves vibrations along the \mathbf{b} -direction, inducing alternating shear deformation, while the other involves vibrations along the \mathbf{a} - and \mathbf{c} -directions, asymmetrically stretching chalcogenide atoms. On the other hand, MoSe₂ shows a very different

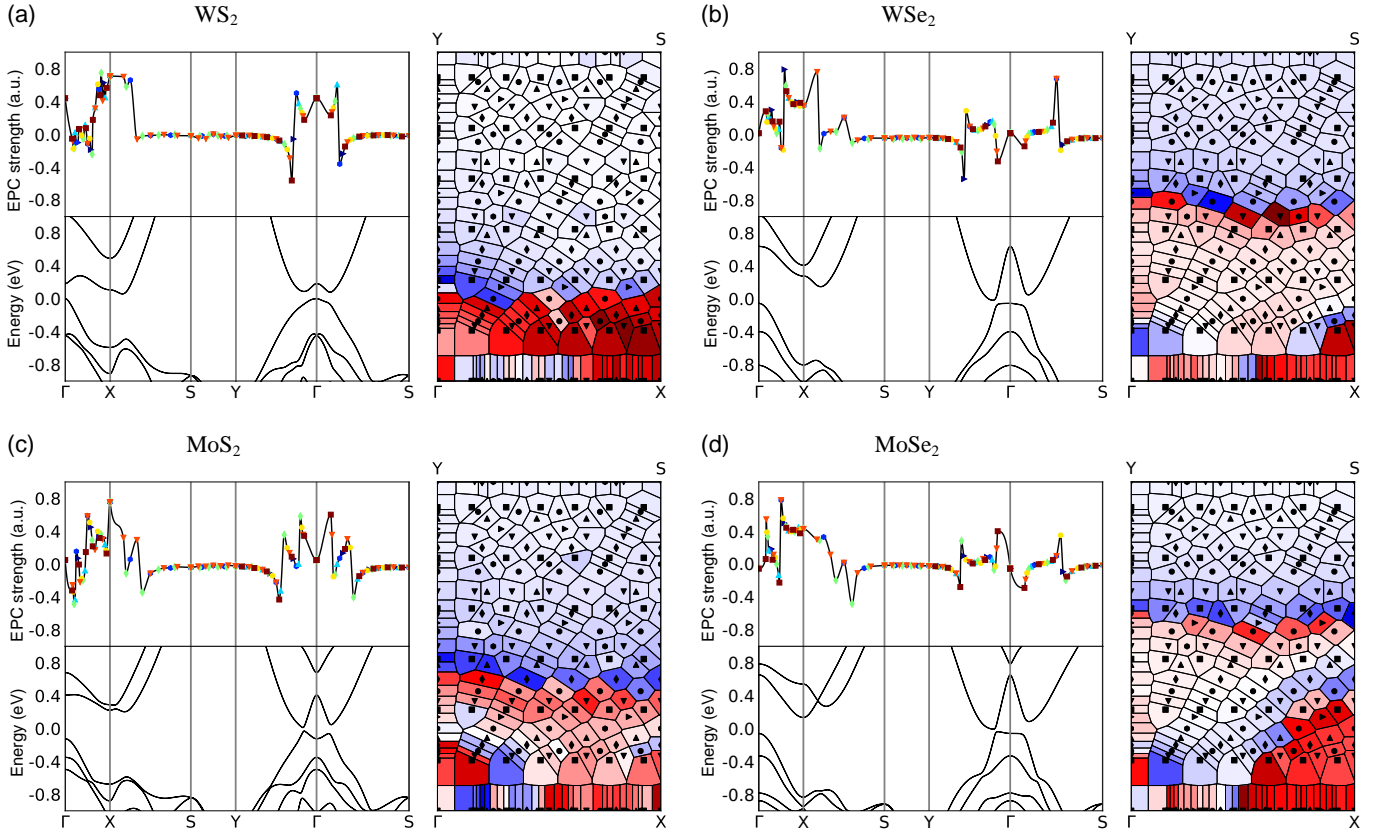


FIG. 5. Electron-phonon coupling strength (left top panel) and band structure (left bottom panel) for (a) WS_2 , (b) WSe_2 , (c) MoS_2 , and (d) MoSe_2 along a high symmetry path in the irreducible Brillouin zone. To calculate the band gap renormalization, the irreducible Brillouin zone is sampled by a non-uniform Farey grid as shown in the right panel, where red and blue represent positive and negative electron-phonon coupling strengths respectively, and the color depth represents the absolute value of the strength.

behaviour, with the strong coupling modes governed by atoms that remain static in the cases of MoS_2 , WS_2 , and WSe_2 . This difference can be attributed to its distinct orbital component. As mentioned earlier, MoS_2 , WS_2 , and WSe_2 display a conduction band at the Γ point that mainly arises from chalcogenide p_y orbitals, whereas in MoSe_2 , it originates from Mo $d_{x^2-y^2}$ and d_{z^2} orbitals. The modes we observe here can bring about a notable alteration in hole density, consequently renormalizing the inverted band gap.

Furthermore, a noteworthy finding is that within WS_2 alone, the inverted band gap shows a nonzero coupling to phonons at the Γ point. The 8th phonon branch with a flat dispersion ($\omega_{\nu, \mathbf{q}} \approx 28$ meV) contributes nearly 73% electron-phonon coupling strength. This unique Γ point contribution drives a larger band gap renormalization at room temperature in WS_2 compared to that of the other three compounds in the TMD family.

Finally, it is also worth noting that the electron-phonon coupling strength curves diverge at some \mathbf{k} -points. This divergence manifests as sharp peaks in the left top panel of Figs. 5(a-d) and visually evident red-blue dividing lines in the right panel. This feature

arises from the double-peak and double-well characteristics of the band structure through the divergence of the electron-phonon coupling strength on the isoenergetic surface. This phenomenon can be rationalized using a perturbation theory framework and has been discussed in the case of bismuthene in Ref. [27]. The computational cost associated with treating the singularity in the electron-phonon coupling strength prevents the calculation of band gap renormalization using the traditional uniform \mathbf{q} -point grid. Therefore, here we have used a Farey grid of order 13, sampling 696 \mathbf{q} -points in the Brillouin zone, corresponding to 12528 modes, to ensure convergence (see Fig. S2 in SM for the detailed convergence tests of band gap renormalization).

2. Long-wavelength phonon-induced band gap renormalization

Given that monolayer $1\text{T}'\text{-MX}_2$ possesses polar chemical bonds between M^{4+} and X^{2-} ions, it is worth examining the band renormalization contributed by long-wavelength phonons (*i.e.* Fröhlich coupling). Table II

	WS ₂	WSe ₂	MoS ₂	MoSe ₂
ω_{LO}	1.26×10^{-3}	9.25×10^{-4}	1.26×10^{-3}	9.13×10^{-4}
ϵ_0	20.2	15.2	18.9	20.9
ϵ_∞	19.4	14.8	18.6	20.5
m_c^*	-0.553	-0.099	-0.127	-0.076
m_v^*	-0.622	-2.034	0.798	27.781
d	11.5	12.2	11.5	12.2
q_0	8.97×10^{-3}	1.11×10^{-2}	9.36×10^{-3}	18.0×10^{-3}
$\Delta E^L(0K)$	-8 meV	-5 meV	-2 meV	-5 meV
$\Delta E^L(300K)$	-8 meV	-5 meV	-1 meV	-5 meV

TABLE II. Material-specific parameters to evaluate the band gap renormalization induced by long-wavelength phonons for WS₂, WSe₂, MoS₂, and MoSe₂. Except for ΔE^L which is in units of meV, the remaining quantities are reported in atomic units, that is, ω_{LO} in units of Hartree, m_c^* and m_v^* in units of the electron mass m_e , d in units of the Bohr radius a_0 , and q_0 in units of $1/a_0$.

summarizes the essential quantities characterizing the Fröhlich interaction and the corresponding band renormalization values calculated at both 0 K and 300 K. We find that the magnitude of the renormalization closely resembles that observed in the case induced by short-wavelength phonons at 0 K. Nevertheless, it is worth noting that the polaron-induced band renormalization exhibits minimal sensitivity to temperature fluctuations. This remarkable temperature independence can be attributed to the very small ionic contribution to the dielectric constant, $\epsilon_0 - \epsilon_\infty \approx 0.5$, across all four considered 2D TMDs. In contrast, HgTe in CdTe/HgTe/CdTe quantum wells (as another realization of topological insulators) have $\epsilon_0 - \epsilon_\infty = 6$ [20], and typical ionic compounds have even larger values [71].

E. Thermal expansion

Now we consider the band gap renormalisation induced by thermal expansion. Due to the 2D materials nature, all of 1T'-MX₂ have weak thermal expansion. The degree of thermal expansion is proportional to the atomic weight, where MoS₂ has the largest thermal expansion, but still does not exceed 0.7% (see Fig. S3 in SM for details).

Figure 4(b) shows the band gap corrections ΔE^{TE} as a function of temperature, while the specific values at both absolute zero and room temperature ($T = 300$ K) are presented in Table I. Overall, the inverted band gaps of all four TMDs decrease as temperature increases. This behavior is expected to some extent, given that thermal expansion drives materials toward their atomic limits, whilst at the same time resulting in a topologically trivial band structure. However, it is worth noting that the band structures of WS₂, MoS₂, and WSe₂ exhibit significant sensitivity to temperature, while MoSe₂ displays limited temperature dependence.

It is important to highlight that our QHA model is

exclusively focused on isotropic thermal expansion. Nevertheless, the established dependence of the band gap in MX₂ under anisotropic strain [15] implies that the inclusion of anisotropic thermal expansion would not qualitatively alter our conclusions.

F. Overall temperature dependence

In the end, we investigate the overall temperature dependence of the inverted band gap. Figure 4(c) shows total band gap corrections as a function of temperature, taking into account the contributions from both electron-phonon coupling and thermal expansion. We find that although WS₂ exhibits the most pronounced electron-phonon coupling, this effect is tempered by substantial thermal expansion, thereby attenuating the band gap renormalization to some extent. In the case of MoS₂, the band gap renormalization reaches a maximum of 3 meV at 300 K. Beyond this point, thermal expansion gains prominence, leading to a reduction in the band gap, *i.e.* the temperature dependence becomes non-monotonic. As for WSe₂, the zero-point motion is outweighed by thermal expansion, leading to a slight decrease in the band gap at 0 K. In comparison, MoSe₂ stands out with the most substantial renormalized band gap when the temperature exceeds 200 K. At room temperature, its band gap renormalization reaches around 15 meV.

IV. INVERSE VARSHNI EFFECT DRIVEN BY BAND INVERSION

Our observations in the four monolayer TMDs show that there seems to be no general trend for the sign of the correction to the band gap in topological insulators: temperature can either promote or suppress the topological phase. This complexity arises from the multiple ways in which temperature can exert its effects, and the competition between these effects is highly contingent upon the very details of the system.

Nevertheless, valuable insights can be gleaned from a very simple model in which electron-phonon coupling itself is indeed conducive to promoting the topological phase when significant band inversion occurs. To illustrate this, let us first consider a normal insulator characterized by parabolic valence and conduction bands at the Γ point where $m_c > 0$ and $m_v < 0$. The band extrema are simply coupled to all other states by a dispersionless phonon with frequency ω_0 . Assuming that the Debye-Waller term is considerably smaller than the Fan-Migdal term (see the definitions in Appendix A), the predominant correction to the band gap occurs near the Γ point where $E_{n\Gamma}^{(0)} - E_{m\Gamma+\mathbf{q}}^{(0)} = \pm \frac{\mathbf{q}^2}{2|m^*|}$ (see Eq. (A6)). The plus/minus sign is for the valence/conduction band, and m^* describes the absolute effective masses. As a result, the temperature dependence of the band gap takes

the form:

$$E_{\text{gap}}(T) = \begin{cases} \frac{-Ce^{\omega_0/(k_B T)}}{e^{\omega_0/(k_B T)} - 1} & \text{for 3D} \\ \frac{A - Be^{\omega_0/(k_B T)}}{e^{\omega_0/(k_B T)} - 1} & \text{for 2D} \end{cases}, \quad (9)$$

where $C > 0$ and $B > A > 0$. The negative sign arises from the opposite curvatures of the valence and conduction bands. This simplified model affords insights into the so-called ‘‘Varshni effect’’ [72] observed in semiconductor physics: the reduction in the energy gap of semiconductors as a function of temperature, a phenomenon observed in the vast majority of insulators.

Interestingly, when applying this same simplified model to an insulator with an inverted band gap, characterized by $m_c < 0$ and $m_v > 0$, we find:

$$E_{\text{gap}}(T) = \begin{cases} \frac{C}{e^{\omega_0/(k_B T)} - 1} & \text{for 3D} \\ \frac{B - Ae^{\omega_0/(k_B T)}}{e^{\omega_0/(k_B T)} - 1} & \text{for 2D} \end{cases}, \quad (10)$$

from which one can anticipate an ‘‘inverse Varshni effect’’. This is particularly relevant because topological insulators often exhibit band inversion with the above band curvature characteristics.

The same argument also holds to the band renormalization induced by Fröhlich coupling (see Eq. (B8)), where the sign of the effective mass of the electrons and holes determines the sign of the renormalization. In a more general manner, one can interpret $g_{mn\nu}(\mathbf{k}, \mathbf{q})$ in Eq. (A6) as $g_{mn\nu}(\mathbf{k}, \mathbf{q}) = g_{mn\nu}^S(\mathbf{k}, \mathbf{q}) + g_{mn\nu}^L(\mathbf{k}, \mathbf{q})$, encompassing both short- and long-wavelength contributions to the electron-phonon coupling matrix element [49]. Thus, we conclude that electron-phonon coupling should broadly promote the topology of systems with a significant band inversion feature.

This insight suggests that the inverse Varshni effect should be more prevalent in topological insulators than in normal insulators. We also note that Garate and Saha reached the same conclusion by considering the renormalization of Dirac mass (instead of the band gap) at finite temperatures [19, 20], while Antonius and Louie further provided a symmetry argument making the picture more nuanced [22].

V. TEMPERATURE-TUNABLE TOPOLOGICAL STATES IN 1T'-WS₂

The strong electron-phonon coupling in 1T'-WS₂ which promotes topology offers a facile mechanism to control the topological order by temperature. To realise this, we consider applying positive biaxial strain to first drive the system to a normal insulator with an uninverted gap. Without considering electron-phonon coupling, we find that the inverted band gap first decreases to zero at

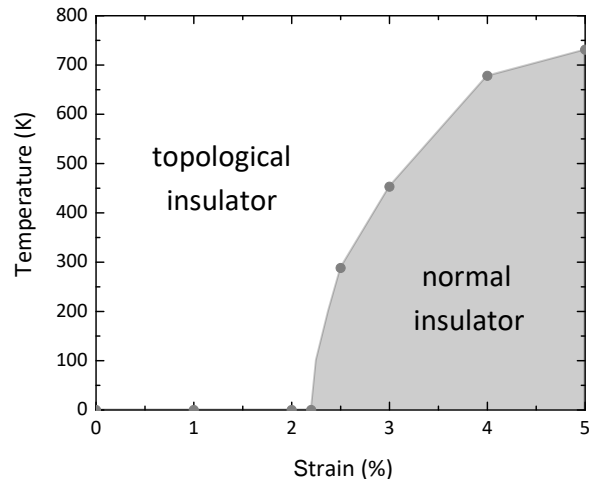


FIG. 6. Temperature-strain phase diagram of WS₂.

strain of 2.2% and then reopens as the strain increases. By explicitly calculating the Z_2 topological invariant, we confirm that this gap-closing indeed induces a topological phase transition associated with the destruction of the edge states.

Figure 6 shows the temperature-strain phase diagram of WS₂. In the range of strain up to 5%, we consistently observe that electron-phonon coupling drives the electronic structure of 1T'-WS₂ toward its topologically non-trivial region. This agrees with the previous theoretical model introduced in Section IV. In particular, we find that at strain of approximately 2.5%, elevating the temperature to 300 K drives a phase transition taking the system from the topologically trivial state imposed by strain to the topologically non-trivial phase. As the first example of temperature promoted topological insulating phases, this temperature-strain tunable state holds promise for tailoring device functionalities.

VI. CONCLUSION

In summary, through first principles calculations, we have elucidated the role of three critical temperature-related factors: electron-phonon coupling, Fröhlich coupling, and thermal expansion, providing a comprehensive examination of the intricate temperature effects in 1T'-MX₂ monolayers.

Our findings demonstrate that within 1T'-MX₂ monolayers electron-phonon coupling generally promotes the topology of the electronic structures. However, the counteracting influence of thermal expansion should not be overlooked, as it generally diminishes the topological attributes and holds the potential to reverse the temperature dependence of the band gap in some cases. This finding also sheds light on using a substrate that can suppress thermal expansion to achieve better thermal robustness

of 2D topological insulators.

Furthermore, our investigation into Fröhlich coupling in 2D materials has revealed its relatively modest temperature dependence within 1T'-MX₂ monolayers due to the small ionic contribution to the dielectric constant. However, the formulation we have found is universal for all 2D materials, which can be useful for understanding the strong band renormalization in the 2D materials that exhibit large ionic contribution to the dielectric constant.

In the context of material science, one of the outcomes of our study is the identification of MoSe₂ as a promising candidate for room temperature applications. It exhibits remarkable resilience against thermal expansion, making it a robust choice for electronic devices operating at higher temperatures. Additionally, WS₂ displays tunable topological behavior under the combined influence of strain and temperature, opening up possibilities for tailored device functionalities. Both materials stand out as novel examples of temperature promoted topological insulators.

Overall, our work advances the fundamental understanding of temperature effects in 1T'-MX₂ monolayers, paving the way for the applications of 2D topological insulators.

ACKNOWLEDGMENTS

S.C. acknowledges financial support from the Cambridge Trust and from the Winton Programme for the Physics of Sustainability. I.J.P. acknowledges financial support from the Worshipful Company of Armourers and Brasiers, Mr Peter Mason, and the Henry Royce Institute. I.J.P. also acknowledges support from Dr Andrew Spencer through the Gonville and Caius College Senior Tutor's Internship grant. B.M. acknowledges support from a UKRI Future Leaders Fellowship (MR/V023926/1), from the Gianna Angelopoulos Programme for Science, Technology, and Innovation, and from the Winton Programme for the Physics of Sustainability. The calculations have been performed using resources provided by the Cambridge Tier-2 system (operated by the University of Cambridge Research Computing Service and funded by EPSRC [EP/P020259/1]), as well as by the UK Materials and Molecular Modelling Hub (partially funded by EPSRC [EP/P020194]), Thomas, and by the UK National Supercomputing Service, ARCHER. Access to Thomas and ARCHER was obtained via the UKCP consortium and funded by EPSRC [EP/P022561/1]).

Appendix A: Real valued phonon displacement operator

Following the procedure that has been described in many textbooks of lattice dynamics [73, 74], we define the normal coordinates $u_{\nu\mathbf{q}}$ from the atomic displacements

$l_{p\alpha j}$ for the phonon system as follows:

$$u_{\nu\mathbf{q}} = \frac{1}{\sqrt{N_p}} \sum_{p\alpha j} \sqrt{m_\alpha} l_{p\alpha j} e^{-i\mathbf{q}\cdot\mathcal{R}_{p\alpha}} \xi_{\nu\mathbf{q}\alpha j}^*, \quad (\text{A1})$$

or inversely,

$$l_{p\alpha j} = \frac{1}{\sqrt{N_p}} \sum_{\nu\mathbf{q}} \frac{1}{\sqrt{m_\alpha}} u_{\nu\mathbf{q}} e^{i\mathbf{q}\cdot\mathcal{R}_{p\alpha}} \xi_{\nu\mathbf{q}\alpha j}, \quad (\text{A2})$$

where p and α run over all primitive cells of the crystal and the ions in the cell respectively, j denotes the Cartesian components, m_α is the mass of the α -th ion, N_p is the number of primitive cells in the crystal, and $\xi_{\nu\mathbf{q}\alpha j}$ is the eigenvector of the dynamical matrix of the system.

It is worth noting that $u_{\nu\mathbf{q}}$ is generally complex (because $\xi_{\nu\mathbf{q}\alpha j}$ is complex), but one can construct a set of real-valued phonon displacement from $u_{\nu\mathbf{q}}$ by partitioning the phonon BZ into three parts:

$$\text{BZ} = \text{BZ}_0 \cup \text{BZ}_{+1} \cup \text{BZ}_{-1}. \quad (\text{A3})$$

Here $\text{BZ}_0 = \{\mathbf{q} \notin \text{BZ}_{\pm 1} \mid \mathbf{q} = -\mathbf{q} \bmod \mathcal{G}\}$ represents a set of discrete \mathbf{q} points invariant under inversion modulo a reciprocal lattice vector (*i.e.* the centre of the Brillouin zone, the centres of its faces, and the corners), and $\text{BZ}_{\pm 1} = \{\mathbf{q} \notin \text{BZ}_0 \mid -\mathbf{q} \in \text{BZ}_{\mp 1}\}$ are mutually inversion symmetric images, each including all the \mathbf{q} -points that are not inversion partners. On this partitioning, we define the real phonon displacement

$$\mu_{\nu\mathbf{q}} = \begin{cases} u_{\nu\mathbf{q}} & \text{for } \mathbf{q} \in \text{BZ}_0 \\ \frac{1}{\sqrt{2}} (u_{\nu\mathbf{q}} + u_{\nu-\mathbf{q}}) & \text{for } \mathbf{q} \in \text{BZ}_{+1} \\ \frac{i}{\sqrt{2}} (u_{\nu\mathbf{q}} - u_{\nu-\mathbf{q}}) & \text{for } \mathbf{q} \in \text{BZ}_{-1} \end{cases}, \quad (\text{A4})$$

or inversely,

$$u_{\nu\mathbf{q}} = \begin{cases} \mu_{\nu\mathbf{q}} & \text{for } \mathbf{q} \in \text{BZ}_0 \\ \frac{1}{\sqrt{2}} (\mu_{\nu\mathbf{q}} + i\mu_{\nu-\mathbf{q}}) & \text{for } \mathbf{q} \in \text{BZ}_{+1} \\ \frac{1}{\sqrt{2}} (\mu_{\nu-\mathbf{q}} - i\mu_{\nu\mathbf{q}}) & \text{for } \mathbf{q} \in \text{BZ}_{-1} \end{cases}. \quad (\text{A5})$$

From Eq. (A4), one can naturally define a real-value phonon differential operator $\frac{\partial}{\partial \mu_{\nu\mathbf{q}}}$, which has been used in the main text to reformulate AHC theory.

We note that one widely used formulation of $E_{n\mathbf{k}}(T)$ is given as follows [75][76]:

$$E_{n\mathbf{k}}(T) = E_{n\mathbf{k}}^{(0)} + \frac{1}{N_p} \sum_{\nu\mathbf{q}} \left[\sum_m \frac{|g_{m\nu\nu}(\mathbf{k}, \mathbf{q})|^2}{E_{n\mathbf{k}}^{(0)} - E_{m\mathbf{k}+\mathbf{q}}^{(0)}} + g_{n\nu\nu}^{\text{DW}}(\mathbf{k}, \mathbf{q}, -\mathbf{q}) \right] \times [1 + 2n_B(\omega_{\nu\mathbf{q}}, T)], \quad (\text{A6})$$

where

$$g_{m\nu\nu}(\mathbf{k}, \mathbf{q}) = \langle \varphi_{m\mathbf{k}+\mathbf{q}} | \partial_{\nu\mathbf{q}} \mathcal{V}_{\text{el}} | \varphi_{n\mathbf{k}} \rangle \quad (\text{A7})$$

is referred to as the standard electron-phonon coupling matrix element, \mathcal{V}_{el} is the potential experienced by the electrons in crystals, and $g_{n\nu\nu'}^{\text{DW}}(\mathbf{k}, \mathbf{q}, -\mathbf{q})$ is a particular case of the Debye-Waller electron-phonon matrix

$$g_{m\nu\nu'}^{\text{DW}}(\mathbf{k}, \mathbf{q}, \mathbf{q}') = \frac{1}{2} \langle \varphi_{m\mathbf{k}+\mathbf{q}+\mathbf{q}'} | \partial_{\nu\mathbf{q}} \partial_{\nu'\mathbf{q}'} \mathcal{H}_{\text{el}} | \varphi_{n\mathbf{k}} \rangle. \quad (\text{A8})$$

Here the (complex) phonon differential operator $\partial_{\nu\mathbf{q}}$ is formulated as [46, 77]

$$\partial_{\nu\mathbf{q}} \equiv \frac{1}{\sqrt{2\omega_{\nu\mathbf{q}}}} \sum_{p\alpha j} \frac{1}{\sqrt{m_{\alpha}}} e^{i\mathbf{q}\cdot\mathcal{R}_{p\alpha}} \xi_{\nu\mathbf{q}\alpha j} \frac{\partial}{\partial l_{p\alpha j}}. \quad (\text{A9})$$

We show that Eq. (2) and Eq. (A6) are equivalent. First, the second derivative term in Eq. (2) can be split into two terms by invoking the Hellmann-Feynman theorem [78], *i.e.*

$$\begin{aligned} \frac{\partial^2 E_{n\mathbf{k}}}{\partial \mu_{\nu\mathbf{q}}^2} &= \left\langle \varphi_{n\mathbf{k}} \left| \frac{\partial^2 \mathcal{H}_{\text{el}}}{\partial \mu_{\nu\mathbf{q}}^2} \right| \varphi_{n\mathbf{k}} \right\rangle + \\ &\left\langle \varphi_{n\mathbf{k}} \left| \frac{\partial \mathcal{H}_{\text{el}}}{\partial \mu_{\nu\mathbf{q}}} \frac{\partial \varphi_{n\mathbf{k}}}{\partial \mu_{\nu\mathbf{q}}} \right\rangle + \left\langle \frac{\partial \varphi_{n\mathbf{k}}}{\partial \mu_{\nu\mathbf{q}}} \left| \frac{\partial \mathcal{H}_{\text{el}}}{\partial \mu_{\nu\mathbf{q}}} \right| \varphi_{n\mathbf{k}} \right\rangle, \end{aligned} \quad (\text{A10})$$

where the derivative of the state can be resolved by an unperturbed complete basis set $\{|\varphi_{n\mathbf{k}}\rangle\}$ according to perturbation theory [79] as follows:

$$\left\langle \frac{\partial \varphi_{n\mathbf{k}}}{\partial \mu_{\nu\mathbf{q}}} \right\rangle = \sum_{\substack{(m, \mathbf{k}') \\ \neq (n, \mathbf{k})}} |\varphi_{m\mathbf{k}'}\rangle \frac{\left\langle \varphi_{m\mathbf{k}'} \left| \frac{\partial \mathcal{H}_{\text{el}}}{\partial \mu_{\nu\mathbf{q}}} \right| \varphi_{n\mathbf{k}} \right\rangle}{E_{n\mathbf{k}}^{(0)} - E_{m\mathbf{k}'}^{(0)}}. \quad (\text{A11})$$

Second, using the chain rule, one can find that the complex phonon differential operator is related to our real-displacement phonon differential operator by the relation

$$\frac{\partial}{\partial \mu_{\nu\mathbf{q}}} = \begin{cases} \sqrt{\frac{2\omega_{\nu\mathbf{q}}}{N_{\text{p}}}} \partial_{\nu\mathbf{q}} & \text{for } \mathbf{q} \in \text{BZ}_0 \\ 2\sqrt{\frac{\omega_{\nu\mathbf{q}}}{N_{\text{p}}}} \partial_{\nu\mathbf{q}} & \text{for } \mathbf{q} \in \text{BZ}_{+1} \\ 0 & \text{for } \mathbf{q} \in \text{BZ}_{-1} \end{cases}, \quad (\text{A12})$$

and thus

$$\lim_{N_{\text{p}} \rightarrow \infty} \sum_{\nu\mathbf{q}} \frac{\partial}{\partial \mu_{\nu\mathbf{q}}} = \lim_{N_{\text{p}} \rightarrow \infty} \sum_{\nu\mathbf{q}} \sqrt{\frac{\omega_{\nu\mathbf{q}}}{N_{\text{p}}}} \partial_{\nu\mathbf{q}}. \quad (\text{A13})$$

Substituting Eqs. (A10) - (A13) into Eq. (2) yields exactly Eq. (A6), so the equivalence is proved. We also note that Refs. [44, 80] derived another formulation of $E_{n\mathbf{k}}(T)$ using a generalized Janak's theorem. Similarly, one can also show that their result

$$E_{n\mathbf{k}}(T) = E_{n\mathbf{k}}^{(0)} + \frac{1}{2N_{\text{p}}} \sum_{\nu\mathbf{q}} \frac{\partial E_{n\mathbf{k}}}{\partial n_{\text{B}}} [1 + 2n_{\text{B}}(\omega_{\nu\mathbf{q}}, T)] \quad (\text{A14})$$

with

$$\begin{aligned} \frac{\partial E_{n\mathbf{k}}}{\partial n_{\text{B}}} &= \frac{1}{2\omega_{\nu\mathbf{q}}} \sum_{p\alpha j} \sum_{p'\alpha'j'} \frac{\partial^2 E_{n\mathbf{k}}}{\partial l_{p\alpha j} \partial l_{p'\alpha'j'}} e^{-i\mathbf{q}\cdot(\mathcal{R}_{p\alpha} - \mathcal{R}_{p'\alpha'})} \\ &\times \frac{\xi_{\nu\mathbf{q}\alpha j}}{\sqrt{m_{\alpha}}} \frac{\xi_{\nu\mathbf{q}\alpha'j'}^*}{\sqrt{m_{\alpha'}}} \end{aligned} \quad (\text{A15})$$

is equivalent to ours.

It is worth noting that the Debye-Waller term involving second-order electron-phonon matrix elements is very challenging to calculate in the density functional perturbation theory framework, therefore one has to invoke the rigid-ion approximation to rewrite it as the product of first-order electron-phonon matrix elements. However, it can be easily included in the finite difference framework as used in this work.

Appendix B: Fröhlich Coupling in 2D

For polar insulators, it has been known that the presence of Fröhlich coupling can play a role in the additional renormalization of the band structure. Here we provide a derivation for this. We start by considering a hole at the Γ point of the conduction band $E_{m\mathbf{q}}^{(0)}$ interacting with a single dispersionless polar longitudinal-optical phonon of frequency ω_{LO} . At a finite temperature T , the self-energy for the hole polaron reads

$$\begin{aligned} \Sigma^{\text{Fr}}(\omega) &= \int \frac{d\mathbf{q}}{\Omega_{\text{BZ}}} |g(\mathbf{q})|^2 \\ &\times \left[\frac{1 - n_{\text{F}}(E_{c\mathbf{q}}^{(0)}, T) + n_{\text{B}}(\omega_{\text{LO}}, T)}{\omega - E_{c\mathbf{q}}^{(0)} - \omega_{\text{LO}} + i\eta} \right. \\ &\left. + \frac{n_{\text{F}}(E_{c\mathbf{q}}^{(0)}, T) + n_{\text{B}}(\omega_{\text{LO}}, T)}{\omega - E_{c\mathbf{q}}^{(0)} + \omega_{\text{LO}} + i\eta} \right]. \end{aligned} \quad (\text{B1})$$

where Ω_{BZ} is the volume of the Brillouin zone, η is a positive infinitesimal, $n_{\text{F}}(E_{c\mathbf{q}}^{(0)}, T) = [\exp(\frac{E_{c\mathbf{q}}^{(0)}}{k_{\text{B}}T}) + 1]^{-1}$ is the Fermi-Dirac factor. The band renormalization arising from $\Sigma^{\text{Fr}}(\omega)$ can be obtained from the standard prescription of many-body perturbation theory:

$$\begin{aligned} E_{c\Gamma}(T) &= E_{c\Gamma}^{(0)} + \int \frac{d\mathbf{q}}{\Omega_{\text{BZ}}} |g(\mathbf{q})|^2 \\ &\times \left[\frac{1 + n_{\text{B}}(\omega_{\text{LO}}, T)}{-|\mathbf{q}|^2 - q_{\text{LO}}^2} + \frac{n_{\text{B}}(\omega_{\text{LO}}, T)}{-|\mathbf{q}|^2 + q_{\text{LO}}^2} \right], \end{aligned} \quad (\text{B2})$$

where we have made the following approximations: (i) the conduction band near the Γ point is isotropic and parabolic, *i.e.* $E_{c\mathbf{q}}^{(0)} = \frac{q^2}{2m^*}$, where m^* is the effective mass; (2) $k_{\text{B}}T \ll E_{c\mathbf{q}}^{(0)}$ thereby $n_{\text{F}}(E_{c\mathbf{q}}^{(0)}, T) = 0$ for all conduction states near the Γ point; (iii) $\Sigma^{\text{Fr}}(\omega)$ is purely real-valued, *i.e.* $i\eta = 0$. In addition, we have defined the effective longitudinal optical wavevector $q_{\text{LO}}^2 = 2m^*\omega_{\text{LO}}$.

We first examine Eq. (B2) in the 3D case, in which the Fröhlich electron-phonon coupling matrix has a long known expression given by [47–49]

$$|g(\mathbf{q})|^2 = \frac{2\pi}{V_{\text{cell}}} \omega_{\text{LO}} \left(\frac{1}{\epsilon_{\infty}} - \frac{1}{\epsilon_0} \right) \frac{1}{|\mathbf{q}|^2}, \quad (\text{B3})$$

where V_{cell} is the volume of the primitive cell, ϵ_{∞} and ϵ_0 are the high-frequency and static relative permittivity. By substituting Eq. (B3) into Eq. (B2) and approximating the Brillouin zone integration as $\int d\mathbf{q} = \int_0^{q_{\text{BZ}}} dq 4\pi q^2 = \Omega_{\text{BZ}}$, we arrive at

$$\begin{aligned} E_{\text{c}\Gamma}(T) &= E_{\text{c}\Gamma}^{(0)} + \int_0^{q_{\text{BZ}}} dq \frac{2}{\pi} m^* \omega_{\text{LO}} \left(\frac{1}{\epsilon_{\infty}} - \frac{1}{\epsilon_0} \right) \\ &\times \left[\frac{1 + n_{\text{B}}(\omega_{\text{LO}}, T)}{-q^2 - q_{\text{LO}}^2} + \frac{n_{\text{B}}(\omega_{\text{LO}}, T)}{-q^2 + q_{\text{LO}}^2} \right] \\ &= E_{\text{c}\Gamma}^{(0)} + \frac{2}{\pi} m^* \omega_{\text{LO}} \left(\frac{1}{\epsilon_{\infty}} - \frac{1}{\epsilon_0} \right) \\ &\times \left[-\frac{1 + n_{\text{B}}(\omega_{\text{LO}}, T)}{q_{\text{LO}}} \tan^{-1} \left(\frac{q_{\text{BZ}}}{q_{\text{LO}}} \right) \right. \\ &\left. + \frac{n_{\text{B}}(\omega_{\text{LO}}, T)}{q_{\text{LO}}} \tanh^{-1} \left(\frac{q_{\text{LO}}}{q_{\text{BZ}}} \right) \right]. \end{aligned} \quad (\text{B4})$$

A frequently employed treatment to further simplify the above expression is to set $q_{\text{BZ}} \rightarrow \infty$, typically leading to an error in the value of the integral of the order of 10% [81]. Following this treatment and considering $T = 0$, we obtain the Fröhlich zero-point band renormalization $\Delta E_{\text{c}\Gamma}^{\text{Fr}}(0) = -\frac{m^* \omega_{\text{LO}}}{q_{\text{LO}}} \left(\frac{1}{\epsilon_{\infty}} - \frac{1}{\epsilon_0} \right) = -\alpha \omega_{\text{LO}}$, where $\alpha = \frac{m^*}{q_{\text{LO}}} \left(\frac{1}{\epsilon_{\infty}} - \frac{1}{\epsilon_0} \right)$ is the dimensionless polaron con-

stant. This outcome aligns precisely with the previously known conclusion about polarons [81].

Now, we move to the 2D case. It is worth noting that unlike the 3D case where the volume element (*i.e.* a spherical shell) $4\pi q^2 dq$ can alleviate the singularity of the integral at $q = 0$, in the 2D case the area element (*i.e.* an annulus) $2\pi q dq$ does not possess the same capability. If one insists on using the Fröhlich electron-phonon coupling matrix given in Eq. (B3) which is proportional to $|\mathbf{q}|^{-2}$, the 2D integral involved in Eq. (B2) will invariably diverge. The primary cause for this divergence can be attributed to the oversimplification of a 2D material, treated merely as a mere sheet lacking thickness, in the modeling of polarons. This has been clearly described in Ref. [52].

To avoid the divergence mentioned above, we employ the recently proposed 2D Fröhlich electron-phonon coupling matrix [51]

$$|g(\mathbf{q})|^2 = \left[\frac{\pi d}{2A_{\text{cell}}} \omega_{\text{LO}} (\epsilon_0 - \epsilon_{\infty}) \right] \frac{q_0^2}{(|\mathbf{q}| + q_0)^2}, \quad (\text{B5})$$

to derive the Fröhlich band renormalization for 2D materials, where A_{cell} is the area of the primitive cell, d is the effective thickness of the 2D material, and q_0 is defined as

$$q_0 = \frac{4\epsilon_{\infty}}{(2\epsilon_{\infty}^2 - 1)d}. \quad (\text{B6})$$

Again, by substituting Eq. (B5) into Eq. (B2) and approximating the Brillouin zone integration as $\int d\mathbf{q} = \int_0^{\infty} dq 2\pi q$, we arrive at

$$\begin{aligned} E_{\text{c}\Gamma}(T) &= E_{\text{c}\Gamma}^{(0)} + \int_0^{\infty} dq \frac{1}{2} m^* q_0^2 d \omega_{\text{LO}} (\epsilon_0 - \epsilon_{\infty}) \frac{q}{(q_0 + q)^2} \left[\frac{1 + n_{\text{B}}(\omega_{\text{LO}}, T)}{-q^2 - q_{\text{LO}}^2} + \frac{n_{\text{B}}(\omega_{\text{LO}}, T)}{-q^2 + q_{\text{LO}}^2} \right] \\ &= E_{\text{c}\Gamma}^{(0)} + \frac{1}{2} m^* q_0^2 d \omega_{\text{LO}} (\epsilon_0 - \epsilon_{\infty}) \left\{ -\frac{q_{\text{LO}}^2 - q_0^2 [2n_{\text{B}}(\omega_{\text{LO}}, T) + 1]}{q_0^4 - q_{\text{LO}}^4} - \frac{\pi q_0 q_{\text{LO}} [n_{\text{B}}(\omega_{\text{LO}}, T) + 1]}{(q_0^2 + q_{\text{LO}}^2)^2} \right. \\ &\quad \left. - \frac{[2q_0^2 (q_0^4 + 3q_{\text{LO}}^4) n_{\text{B}}(\omega_{\text{LO}}, T) + (q_0^2 - q_{\text{LO}}^2)^3] [\ln(q_0) - \ln(q_{\text{LO}})]}{(q_0^4 - q_{\text{LO}}^4)^2} \right\}. \end{aligned} \quad (\text{B7})$$

In a similar manner, one can find the expression for the correction to the valence band $E_{\text{v}\Gamma}(T)$.

Invoking the adiabatic approximation by replacing the term in the bracket of Eq. (3) by $[2n_{\text{B}}(\omega_{\text{LO}}, T) + 1]/(-q^2 + i2m^*\eta)$ and then taking the real part [50], we obtain:

$$\begin{aligned}
E_{c\Gamma}(T) &= E_{c\Gamma}^{(0)} + \Re \left\{ \int_0^\infty dq \frac{1}{2} m^* q_0^2 d\omega_{LO} (\epsilon_0 - \epsilon_\infty) \frac{q}{(q_0 + q)^2} \frac{2n_B(\omega_{LO}, T) + 1}{-q^2 + i2m^*\eta} \right\} \\
&= E_{c\Gamma}^{(0)} + \frac{1}{8} m^* q_0^2 d\omega_{LO} (\epsilon_0 - \epsilon_\infty) [2n_B(\omega_{LO}, T) + 1] \\
&\times \Re \left\{ -\frac{2(\pi - 4i)m^*\eta - (4 - 4i)\pi q_0 \sqrt{m^*\eta}}{(2m^*\eta + iq_0^2)^2} - \frac{(4 - i\pi)q_0^2 + 2(q_0^2 + i2m^*\eta) [\ln(2m^*\eta/q_0^2)]}{(2m^*\eta + iq_0^2)^2} \right\}
\end{aligned} \tag{B8}$$

It is worth noting that the small imaginary component $i\eta$ introduced here is *ad hoc* rather than *ab initio*. The physical meaning of η can be inferred as a finite lifetime for the unoccupied electronic states due to thermal effects. In principle, in more accurate approaches the

η should be replaced by the finite physical linewidth of electrons. As already pointed out by Ref. [80], decreasing η does not lead to convergence for polar materials. One has to treat this with caution in band renormalization calculations.

-
- [1] C. L. Kane and E. J. Mele, “ Z_2 topological order and the quantum spin Hall effect,” *Phys. Rev. Lett.* **95**, 146802 (2005).
- [2] C. L. Kane and E. J. Mele, “Quantum spin Hall effect in graphene,” *Phys. Rev. Lett.* **95**, 226801 (2005).
- [3] B. A. Bernevig, T. L. Hughes, and S. Zhang, “Quantum spin Hall effect and topological phase transition in hgte quantum wells,” *Science* **314**, 1757–1761 (2006).
- [4] M. Z. Hasan and C. L. Kane, “Colloquium: Topological insulators,” *Rev. Mod. Phys.* **82**, 3045–3067 (2010).
- [5] Xiao-Liang Qi and Shou-Cheng Zhang, “Topological insulators and superconductors,” *Rev. Mod. Phys.* **83**, 1057–1110 (2011).
- [6] A. Bansil, Hsin Lin, and Tanmoy Das, “Colloquium: Topological band theory,” *Rev. Mod. Phys.* **88**, 021004 (2016).
- [7] N. P. Armitage, E. J. Mele, and Ashvin Vishwanath, “Weyl and Dirac semimetals in three-dimensional solids,” *Rev. Mod. Phys.* **90**, 015001 (2018).
- [8] B. Q. Lv, T. Qian, and H. Ding, “Experimental perspective on three-dimensional topological semimetals,” *Rev. Mod. Phys.* **93**, 025002 (2021).
- [9] D. Hsieh, D. Qian, L. Wray, Y. Xia, Y. S. Hor, R. J. Cava, and M. Z. Hasan, “A topological Dirac insulator in a quantum spin Hall phase,” *Nature* **452**, 970–974 (2008).
- [10] S. Xu, Y. Xia, L. A. Wray, S. Jia, F. Meier, J. H. Dil, J. Osterwalder, B. Slomski, A. Bansil, H. Lin, R. J. Cava, and M. Z. Hasan, “Topological phase transition and texture inversion in a tunable topological insulator,” *Science* **332**, 560–564 (2011).
- [11] X. Xi, C. Ma, Z. Liu, Z. Chen, W. Ku, H. Berger, C. Martin, D. B. Tanner, and G. L. Carr, “Signatures of a pressure-induced topological quantum phase transition in BiTeI,” *Phys. Rev. Lett.* **111**, 155701 (2013).
- [12] A. Bera, K. Pal, D. V. S. Muthu, S. Sen, P. Guptasarma, U. V. Waghmare, and A. K. Sood, “Sharp Raman anomalies and broken adiabaticity at a pressure induced transition from band to topological insulator in Sb2Se3,” *Phys. Rev. Lett.* **110**, 107401 (2013).
- [13] Y. Liu, Y. Y. Li, S. Rajput, D. Gilks, L. Lari, P. L. Galindo, V. K. Weinert, M. Lazarov, and V. K. Li, “Tuning Dirac states by strain in the topological insulator Bi2Se3,” *Nat. Phys.* **10**, 294–299 (2014).
- [14] S. Liu, Y. Kim, L. Z. Tan, and A. M. Rappe, “Strain-induced ferroelectric topological insulator,” *Nano Lett.* **16**, 1663–1668 (2016).
- [15] Xianqing Lin and Jun Ni, “Topological phase transition due to strain-controlled evolution of the inverted bands in 1T’-MX2,” *Phys. Rev. B* **95**, 245436 (2017).
- [16] M. Kim, C. H. Kim, H. Kim, and J. Ihm, “Topological quantum phase transitions driven by external electric fields in Sb2Te3 thin films,” *Proc. Natl. Acad. Sci* **109**, 671–674 (2012).
- [17] T. Zhang, J. Ha, N. Levy, Y. Kuk, and J. Stroscio, “Electric-field tuning of the surface band structure of topological insulator Sb2Te3 thin films,” *Phys. Rev. Lett.* **111**, 056803 (2013).
- [18] Xianqing Lin and Jun Ni, “Switch effect of the non-quantized intrinsic spin Hall conductivity in monolayered monoclinic transition metal dichalcogenides,” *J. Condens. Matter Phys.* **29**, 295302 (2017).
- [19] I. Garate, “Phonon-induced topological transitions and crossovers in Dirac materials,” *Phys. Rev. Lett.* **110**, 046402 (2013).
- [20] K. Saha and I. Garate, “Phonon-induced topological insulation,” *Phys. Rev. B* **89**, 205103 (2014).
- [21] Bartomeu Monserrat and David Vanderbilt, “Temperature effects in the band structure of topological insulators,” *Phys. Rev. Lett.* **117**, 226801 (2016).
- [22] Gabriel Antonius and Steven G. Louie, “Temperature-induced topological phase transitions: Promoted versus suppressed nontrivial topology,” *Phys. Rev. Lett.* **117**, 246401 (2016).
- [23] Bartomeu Monserrat and Awadhesh Narayan, “Unraveling the topology of ZrTe5 by changing temperature,” *Phys. Rev. Res.* **1**, 033181 (2019).
- [24] Bo Peng, Ivona Bravić, Judith L. MacManus-Driscoll, and Bartomeu Monserrat, “Topological semimetallic phase in PbO2 promoted by temperature,” *Phys. Rev. B* **100**, 161101 (2019).
- [25] Véronique Brousseau-Couture, Gabriel Antonius, and Michel Côté, “Temperature dependence of the topological phase transition of BiTeI from first principles,” *Phys. Rev. Res.* **2**, 023185 (2020).
- [26] José D. Querales-Flores, Pablo Aguado-Puente, Đorđe Dangić, Jiang Cao, Piotr Chudzinski, Tchavdar N.

- Todorov, Myrta Grüning, Stephen Fahy, and Ivana Savić, “Towards temperature-induced topological phase transition in SnTe: A first-principles study,” *Phys. Rev. B* **101**, 235206 (2020).
- [27] Siyu Chen, Pascal T. Salzbrenner, and Bartomeu Monserrat, “Nonuniform grids for brillouin zone integration and interpolation,” *Phys. Rev. B* **106**, 155102 (2022).
- [28] Antimo Marrazzo, “Thermal robustness of the quantum spin Hall phase in monolayer WTe₂,” *Phys. Rev. Mater.* **7**, L021201 (2023).
- [29] Steffen Wiedmann, Andreas Jost, Cornelius Thienel, Christoph Brüne, Philipp Leubner, Hartmut Buhmann, Laurens W. Molenkamp, J. C. Maan, and Uli Zeitler, “Temperature-driven transition from a semiconductor to a topological insulator,” *Phys. Rev. B* **91**, 205311 (2015).
- [30] Bastian M Wojek, MH Berntsen, Viktor Jonsson, A Szczerbakow, P Dziawa, BJ Kowalski, T Story, and Oscar Tjernberg, “Direct observation and temperature control of the surface Dirac gap in a topological crystalline insulator,” *Nat. Commun* **6**, 8463 (2015).
- [31] S. Thirupathiah, Rajveer Jha, Banabir Pal, J. S. Matias, P. Kumar Das, I. Vobornik, R. A. Ribeiro, and D. D. Sarma, “Temperature-independent band structure of WTe₂ as observed from angle-resolved photoemission spectroscopy,” *Phys. Rev. B* **96**, 165149 (2017).
- [32] Ayelet Notis Berger, Erick Andrade, Alexander Kerelsky, Drew Edelberg, Jian Li, Zhijun Wang, Lunyong Zhang, Jaewook Kim, Nader Zaki, Jose Avila, *et al.*, “Temperature-driven topological transition in 1T'-MoTe₂,” *npj Quantum Materials* **3**, 2 (2018).
- [33] Y. J. Chen, L. X. Xu, J. H. Li, Y. W. Li, H. Y. Wang, C. F. Zhang, H. Li, Y. Wu, A. J. Liang, C. Chen, S. W. Jung, C. Cacho, Y. H. Mao, S. Liu, M. X. Wang, Y. F. Guo, Y. Xu, Z. K. Liu, L. X. Yang, and Y. L. Chen, “Topological electronic structure and its temperature evolution in antiferromagnetic topological insulator MnBi₂Te₄,” *Phys. Rev. X* **9**, 041040 (2019).
- [34] Sabin Regmi, M. Mofazzel Hosen, Barun Ghosh, Bahadur Singh, Gyanendra Dhakal, Christopher Sims, Baokai Wang, Firoza Kabir, Klauss Dimitri, Yangyang Liu, Amit Agarwal, Hsin Lin, Dariusz Kaczorowski, Arun Bansil, and Madhab Neupane, “Temperature-dependent electronic structure in a higher-order topological insulator candidate EuIn₂As₂,” *Phys. Rev. B* **102**, 165153 (2020).
- [35] D. A. Estyunin, I. I. Klimovskikh, A. M. Shikin, E. F. Schwier, M. M. Otrokov, A. Kimura, S. Kumar, S. O. Filinov, Z. S. Aliev, M. B. Babanly, and E. V. Chulkov, “Signatures of temperature driven antiferromagnetic transition in the electronic structure of topological insulator MnBi₂Te₄,” *APL Materials* **8**, 021105 (2020).
- [36] Yuxuan Jiang, Tianhao Zhao, LuoJia Zhang, Qiang Chen, Haidong Zhou, Mykhaylo Ozerov, Dmitry Smirnov, and Zhigang Jiang, “Revealing temperature evolution of the Dirac band in ZrTe₅ via magnetoinfrared spectroscopy,” *Phys. Rev. B* **108**, L041202 (2023).
- [37] I. Mohelsky, J. Wyzula, B. A. Piot, G. D. Gu, Q. Li, A. Akrap, and M. Orlita, “Temperature dependence of the energy band gap in ZrTe₅: Implications for the topological phase,” *Phys. Rev. B* **107**, L041202 (2023).
- [38] Xiaofeng Qian, Junwei Liu, Liang Fu, and Ju Li, “Quantum spin Hall effect in two-dimensional transition metal dichalcogenides,” *Science* **346**, 1344–1347 (2014).
- [39] Shujie Tang, Chaofan Zhang, Dillon Wong, Zahra Pedramrazi, Hsin-Zon Tsai, Chunjing Jia, Brian Moritz, Martin Claassen, Hyejin Ryu, Salman Kahn, *et al.*, “Quantum spin Hall state in monolayer 1T'-WTe₂,” *Nat. Phys.* **13**, 683–687 (2017).
- [40] Shuichi Murakami, Satoshi Iso, Yshai Avishai, Masaru Onoda, and Naoto Nagaosa, “Tuning phase transition between quantum spin hall and ordinary insulating phases,” *Phys. Rev. B* **76**, 205304 (2007).
- [41] P.B. Allen and V. Heine, “Theory of the temperature dependence of electronic band structures,” *J Phys C Solid State Phys* **9**, 2305–2312 (1976).
- [42] P. B. Allen and M. Cardona, “Theory of the temperature dependence of the direct gap of germanium,” *Phys. Rev. B* **23**, 1495–1505 (1981).
- [43] P. B. Allen and M. Cardona, “Temperature dependence of the direct gap of Si and Ge,” *Phys. Rev. B* **27**, 4760–4769 (1983).
- [44] S. Poncé, G. Antonius, Y. Gillet, P. Boulanger, J. Laflamme Janssen, A. Marini, M. Côté, and X. Gonze, “Temperature dependence of electronic eigenenergies in the adiabatic harmonic approximation,” *Phys. Rev. B* **90**, 214304 (2014).
- [45] Bartomeu Monserrat, “Electron–phonon coupling from finite differences,” *J. Condens. Matter Phys.* **30**, 083001 (2018).
- [46] F. Giustino, “Electron-phonon interactions from first principles,” *Rev. Mod. Phys.* **89**, 015003 (2017).
- [47] H. Fröhlich, H. Pelzer, and S. Zienau, “Xx. properties of slow electrons in polar materials,” *Lond.Edinb.Dubl.Phil.Mag* **41**, 221–242 (1950).
- [48] H. Fröhlich, “Electrons in lattice fields,” *Advances in Physics* **3**, 325–361 (1954).
- [49] Carla Verdi and Feliciano Giustino, “Fröhlich electron-phonon vertex from first principles,” *Phys. Rev. Lett.* **115**, 176401 (2015).
- [50] Jean Paul Nery and Philip B. Allen, “Influence of Fröhlich polaron coupling on renormalized electron bands in polar semiconductors: Results for zinc-blende GaN,” *Phys. Rev. B* **94**, 115135 (2016).
- [51] Weng Hong Sio and Feliciano Giustino, “Unified ab initio description of Fröhlich electron-phonon interactions in two-dimensional and three-dimensional materials,” *Phys. Rev. B* **105**, 115414 (2022).
- [52] Weng Hong Sio and Feliciano Giustino, “Polarons in two-dimensional atomic crystals,” *Nat. Phys.* , 1–8 (2023).
- [53] Jonathan H. Lloyd-Williams and Bartomeu Monserrat, “Lattice dynamics and electron-phonon coupling calculations using nondiagonal supercells,” *Phys. Rev. B* **92**, 184301 (2015).
- [54] G. Leibfried and W. Ludwig, “Theory of anharmonic effects in crystals,” *Solid State Physics*, **12**, 275–444 (1961).
- [55] Anjali Singh, Sharmila N Shirodkar, and Umesh V Waghmare, “1H and 1T polymorphs, structural transitions and anomalous properties of (Mo,W)(S,Se)₂ monolayers: first-principles analysis,” *2D Mater.* **2**, 035013 (2015).
- [56] Stanley S Chou, Na Sai, Ping Lu, Eric N Coker, Sheng Liu, Kateryna Artyushkova, Ting S Luk, Bryan Kaehr, and C Jeffrey Brinker, “Understanding catalysis in a multiphasic two-dimensional transition metal dichalcogenide,” *Nat. Commun* **6**, 8311 (2015).
- [57] P. Hohenberg and W. Kohn, “Inhomogeneous electron gas,” *Phys. Rev.* **136**, B864–B871 (1964).

- [58] W. Kohn and L. J. Sham, “Self-consistent equations including exchange and correlation effects,” *Phys. Rev.* **140**, A1133–A1138 (1965).
- [59] G. Kresse and J. Furthmüller, “Efficiency of ab-initio total energy calculations for metals and semiconductors using a plane-wave basis set,” *Comput. Mater. Sci.* **6**, 15 – 50 (1996).
- [60] P. E. Blöchl, “Projector augmented-wave method,” *Phys. Rev. B* **50**, 17953–17979 (1994).
- [61] G. Kresse and D. Joubert, “From ultrasoft pseudopotentials to the projector augmented-wave method,” *Phys. Rev. B* **59**, 1758–1775 (1999).
- [62] John P. Perdew, Kieron Burke, and Matthias Ernzerhof, “Generalized gradient approximation made simple,” *Phys. Rev. Lett.* **77**, 3865–3868 (1996).
- [63] D. D. Koelling and B. N. Harmon, “A technique for relativistic spin-polarised calculations,” *J. Phys. C: Solid State Phys.* **10**, 3107 (1977).
- [64] Miguel M Ugeda, Artem Pulkin, Shujie Tang, Hyejin Ryu, Quansheng Wu, Yi Zhang, Dillon Wong, Zahra Pedramrazi, Ana Martín-Recio, Yi Chen, *et al.*, “Observation of topologically protected states at crystalline phase boundaries in single-layer WSe₂,” *Nat. Commun* **9**, 3401 (2018).
- [65] Hai Xu, Dong Han, Yang Bao, Fang Cheng, Zijing Ding, Sherman JR Tan, and Kian Ping Loh, “Observation of gap opening in 1T’ phase MoS₂ nanocrystals,” *Nano Lett.* **18**, 5085–5090 (2018).
- [66] P Chen, Woei Wu Pai, Y-H Chan, W-L Sun, C-Z Xu, D-S Lin, MY Chou, A-V Fedorov, and T-C Chiang, “Large quantum-spin-Hall gap in single-layer 1 T’ WSe₂,” *Nat. Commun* **9**, 2003 (2018).
- [67] Line Jelver, Daniele Stradi, Kurt Stokbro, Thomas Olsen, and Karsten Wedel Jacobsen, “Spontaneous breaking of time-reversal symmetry at the edges of 1T’ monolayer transition metal dichalcogenides,” *Phys. Rev. B* **99**, 155420 (2019).
- [68] J Cayssol and J N Fuchs, “Topological and geometrical aspects of band theory,” *J. Phys. Materials* **4**, 034007 (2021).
- [69] Lixuan Xu, Yiwei Li, Yuqiang Fang, Huijun Zheng, Wujun Shi, Cheng Chen, Ding Pei, Donghui Lu, Makoto Hashimoto, Meixiao Wang, Lexian Yang, Xiao Feng, Haijun Zhang, Fuqiang Huang, Qikun Xue, Ke He, Zhongkai Liu, and Yulin Chen, “Topology hierarchy of transition metal dichalcogenides built from quantum spin Hall layers,” *Adv. Mater.* **35**, 2300227 (2023).
- [70] Biswapriyo Das, Diptiman Sen, and Santanu Mahapatra, “Tuneable quantum spin Hall states in confined 1T’ transition metal dichalcogenides,” *Sci. Rep.* **10**, 6670 (2020).
- [71] Walter R. L. Lambrecht, Churna Bhandari, and Mark van Schilfgaarde, “Lattice polarization effects on the screened coulomb interaction W of the GW approximation,” *Phys. Rev. Mater.* **1**, 043802 (2017).
- [72] Y.P. Varshni, “Temperature dependence of the energy gap in semiconductors,” *Physica* **34**, 149–154 (1967).
- [73] Max Born, Kun Huang, and M Lax, *Dynamical theory of crystal lattices* (Oxford University Press, 1955).
- [74] Martin T Dove, *Introduction to lattice dynamics* (Cambridge University Press, 1993).
- [75] F. Giustino, S. G. Louie, and M. L. Cohen, “Electron-phonon renormalization of the direct band gap of diamond,” *Phys. Rev. Lett.* **105**, 265501 (2010).
- [76] The sum excludes $\mathbf{q} = \mathbf{0}$ for the first term in $\sum_{\nu\mathbf{q}}[\dots]$ when $m = n$.
- [77] F. Giustino, M. L. Cohen, and S. G. Louie, “Electron-phonon interaction using wannier functions,” *Phys. Rev. B* **76**, 165108 (2007).
- [78] B.M. Deb, “Note on an upper bound property of second derivatives of the energy,” *Chem. Phys. Lett.* **17**, 78 – 79 (1972).
- [79] S. Baroni, S. de Gironcoli, A. Dal Corso, and P. Giannozzi, “Phonons and related crystal properties from density-functional perturbation theory,” *Rev. Mod. Phys.* **73**, 515–562 (2001).
- [80] S. Poncé, Y. Gillet, J. Laflamme Janssen, A. Marini, M. Verstraete, and X. Gonze, “Temperature dependence of the electronic structure of semiconductors and insulators,” *J. Chem. Phys.* **143**, 102813 (2015).
- [81] Joseph Callaway, *Quantum theory of the solid state* (Academic Press, 1976).